Brain Tissue Context for Enhancing Brain Tumor Segmentation: a Contribution to BraTS 2025

Mehdi Astaraki[1,2,3], Farangis Sajadi Moghadam[4], and Iuliana Toma-Dasu[1,2]

[1] Department of Medical Radiation Physics, Stockholm University, Solna, Sweden
[2] Department of Oncology-Pathology, Karolinska Institutet, Solna, Sweden
[3] Department of Clinical Science, Intervention and Technology, Karolinska Institutet, Huddinge, Sweden
[4] Department of Biomedical Engineering, Amirkabir University of Technology, Tehran, Iran

Abstract. The development of deep learning methodologies has significantly impacted medical image segmentation, leading to highly accurate models for critical applications such as brain tumor delineation in MRI volumes. Precise tumor segmentation is indispensable for quantitative analysis, surgical planning, radiation treatment delivery, and disease monitoring. This paper presents a novel context-aware segmentation pipeline, conceptually rooted in anomaly detection, by integrating brain tissues as an auxiliary segmentation class. This inclusion enhances the discriminability between pathological and healthy tissues. To mitigate the class imbalance inherent in this added segmentation scheme, we incorporated a class-adaptive loss function within the nnU-Net and MedNeXt frameworks. The efficacy of this approach was rigorously evaluated on five tasks within the Brain Tumor Segmentation (*BraTS*) 2025 MICCAI Lighthouse challenge: adult glioma (*GLI*), pediatric glioma (*PED*), brain metastasis (*MET*), meningioma in pre-operative (*MENpre*), and meningioma in treatment planning (*MENrt*) segmentation. Our method demonstrated promising overall whole tumor segmentation performance on the validation set, yielding lesion-wise Dice scores of 0.873 (*GLI*), 0.945 (*PED*), 0.861 (*MENpre*), 0.845 (*MENrt*), and 0.679 (*MET*).

Keywords: brain tumor, MRI, segmentation, brats challenge

1 Introduction

Brain tumors, though constituting a relatively infrequent oncological diagnosis, impose a substantial burden of morbidity and mortality across the demographic spectrum. These heterogeneous neoplasms are broadly categorized into primary brain tumors, originating within the *central nervous system (CNS)* parenchyma, and secondary or metastatic tumors, which represent extracranial malignancies that have disseminated to the brain [30]. This inherent diversity manifests deeply in their genetic, histological, and ultimately, their characteristic imaging signatures [11]. Their imaging pattern is notably inhomogeneous, frequently comprising extensive necrotic regions, vigorously enhancing vital tumor components, and substantial peritumoral edema.

Magnetic Resonance Imaging (MRI) serves as the indispensable imaging modality for brain tumor screening, owing to its unparalleled capacity to generate high-resolution images of cerebral soft tissues [25]. These images are critically important for accurate diagnostic assessment, *radiotherapy (RT)* planning, and disease monitoring. In clinical practice, *multi-parametric MRI (mpMRI)* sequences are routinely employed to characterize the heterogeneous subregions of brain tumors, each exhibiting distinct signal intensities across various *MRI* pulse sequences. The intrinsic variability and complex morphology of these tumors render their manual assessment and delineation a technically demanding and exceedingly time-consuming endeavor. Accurate and consistent delineation of brain tumors is paramount for precise diagnosis and *RT* planning; however, this task is widely recognized as labor-intensive and susceptible to both inter-observer and intra-observer variability [9]. Hence, the development of automated tumor segmentation algorithms in *MRI* emerges as a clinically transformative tool capable of supporting surgical planning, optimizing *RT* dosimetry, and facilitating objective and quantitative assessment of treatment response.

Advances in *Deep Learning (DL)* methodologies resulted in the emergence of numerous computational models for brain tumor segmentation, predominantly utilizing institutional datasets. Nevertheless, the systematic benchmarking and comparative performance analysis of these diverse strategies have historically been impeded by several confounding factors. These include variations in the specific imaging modalities employed (e.g., structural *MRI* vs. multi-modal CT-*MRI* combinations), differences in the investigated brain tumor types (e.g., high-grade vs. low-grade gliomas), and inconsistencies in the evaluation criteria applied (e.g., subject-wise overlapping metrics vs. lesion-wise distance metrics).

To overcome these significant limitations, the *Brain Tumor Segmentation (BraTS)* challenge was established in the Medical Image Computing and Computer Assisted Intervention (MICCAI) 2012 conference. The primary objective of *BraTS* was to facilitate the objective and standardized evaluation of state-of-the-art algorithms for automated brain tumor segmentation in *MRI*. Specifically, for each annual MICCAI conference, *BraTS* organizers have consistently provided a carefully examined collection of structural *MRI* scans, *native T1-weighted (T1n)*, *contrast enhanced T1-weighted (T1c)*, *T2-weighted (T2w)*, and *T2-weighted fluid-attenuated inversion recovery (T2f)* images, accompanied by corresponding expert-generated segmentation masks [26, 3, 16].

Initially centered on segmenting *glioma (GLI)* in pre-operative *MRI*, the *BraTS* challenge has significantly broadened its scope. It now includes a wider array of segmentation tasks, such as post-treatment *GLI*, *meningioma (MEN)* (pre- and post-*RT*), *pediatric (PED)* brain tumors, brain *metastasis (MET)*, and gliomas in *Sub-Saharan African populations (SSA)*.

The remarkable advancements in *DL* techniques have deeply facilitated the development of robust algorithms for automated brain tumor segmentation. Inspired by groundbreaking architectures such as the U-Net [32] and V-Net [27], a multitude of encoder-decoder models have been subsequently developed for diverse segmentation tasks. These models primarily introduce innovations through

architectural modifications and/or refined optimization procedures. Several *Convolutional Neural Network (CNN)*, transformer-based models, and recently State Space Sequence Models including U-Mamba [23], STU-Net [12], U-Net++ [38], SegResNet [29], nn-UNet [14], MedNeXt [34], Swin UNetR [10], have recently demonstrated superior performance in the challenging domain of brain tumor segmentation.

Previous years' top-performing algorithms in brain tumor segmentation have consistently utilized a diverse array of methodologies, encompassing sophisticated preprocessing techniques, various segmentation network architectures, and refined post-processing strategies. For example, the winning solution for BraTS GLI in both 2023 and 2024 leveraged a generative model in conjunction with image registration techniques [7]. This approach significantly augmented the volume of training data, which was then used to train nnU-Net and Swin UNETR models. Subsequent stages involved thresholding and model ensemble methods to refine the segmentation output. Similarly, the winner of BraTS GLI 2022 developed an ensemble of three distinct segmentation models: DeepSeg, DeeoSCAN, and a modified nnU-Net, with the final segmentation generated using the STAPLE algorithm [37]. The BraTS GLI 2021 winner, in contrast, focused on architectural modifications to the nnU-Net model, specifically by increasing the number of filters within its encoder and bottleneck sections while retaining the original decoder structure [22].

Our proposed approach for segmenting various brain tumor entities in the BraTS 2025 cluster of challenges integrates healthy brain tissue as an additional segmentation label. This inclusion aims to enrich the learning process by providing crucial anatomical context. Hence, we have expanded the number of segmentation classes to incorporate healthy brain tissues and employ several robust segmentation pipelines, including nnU-Net, and MedNeXt for the *GLI*, *PED*, *MET*, and *MEN* tasks.

2 Materials and Methods

This study utilized annotated multi-modal *MRI* datasets provided through the MICCAI *BraTS* 2025 Lighthouse Challenge, comprising five segmentation tasks: adult *GLI*, pre-operative *MEN*, *MEN* radiotherapy, brain *MET*, and *PED* tumors. All datasets were distributed in Neuroimaging Informatics Technology Initiative (NIfTI) via the Synapse platform.

2.1 Studied Dataset

Task 1: Adult Glioma (GLI) – This dataset consists of pre- and post-treatment scans from 2601 training, and 407 validation subjects [1, 2, 5]. Each case includes four *mpMRI* sequences: *T1n*, *T1c*, *T2w*, and *T2f*. Segmentation annotations covered four tumor subregions: *Enhancing tumor (ET)*, *non-enhancing tumor core (NETC)*, *surrounding non-enhancing FLAIR hyperintensity (SNFH)*, and *resection cavity (RC)*. Combined regions including *tumor core (TC)* and

Whole tumor (WT) are defined, respectively, *ET* plus *NETC* and the union of *ET*, *NETC*, and *SNFH*. The provided dataset underwent rigorous preprocessing, including coregistration of all sequences, skull stripping for non-brain tissue removal, and rigid registration to the Montreal Neurological Institute (MNI) atlas space [8].

Task 2: Pre-operative Meningioma (MEN-pre) – This dataset comprises 1000 training, and 141 validation of *mpMRI*s including *T1n*, *T1c*, *T2w*, and *T2f* [20]. Tumor annotations delineate the following constituent subregions: *ET*, *NETC*, and *SNFH*. The dataset was released after applying several preprocessing steps, including coregistration of all sequences, skull stripping, and rigid registration to the SRI24 atlas space [31].

Task 3: Meningioma Radiotherapy (MEN-rt) – Designed for *RT* planning, this task contains 500 training, and 70 validation [21]. Each subject is provided with a single 3D *T1c* sequence alongside a binary mask representing the *gross tumor volume (GTV)*. Crucially, each *MRI* scan is provided in its native anatomical space, without prior image preprocessing steps such as normalization to an atlas space.

Task 4: Brain Metastases (MET) – This dataset includes 1296 labeled training, and 179 validation subjects [28, 24]. Each subject contains four *MRI* sequences (*T1n*, *T1c*, *T2w*, *T2f*) with segmentation labels of *ET*. *NETC*, *RC*, and *SNFH*. The majority of the data underwent preprocessing, which included coregistration of all sequences, skull-stripping, and registration to the SRI24 atlas space. However, a subset of the data was provided with coregistration and skull-stripping but remained in its native anatomical space.

Task 6: Pediatric Tumors (PED) – This dataset provides 261 training, and 91 validation cases [18, 19]. Similar to other tasks with *mpMRI* scans, each subject includes the four standard sequences. Segmentation labels consist of *ET*, *NETC*, *Cystic component (CC)*, and *edema (ED)*. The preprocessing step of this dataset includes the coregistration of sequences, registration to SRI24 atlas space, and defacing.

2.2 Methods

Preprocessing: Prior to model training, image preprocessing was executed in two distinct stages. The initial stage focused on optimizing patch extraction for subsequent network input. This involved cropping MRI volumes to maximally exclude background regions. A series of thresholding and connected component analysis steps were employed to segment the volumes into foreground (body) and background, with the body's skin serving as the anatomical boundary. Following this segmentation, a bounding box was generated to encompass the widest portion of the volume. This cropping approach facilitated the optimal loading of relevant brain tissues within each patch, thereby effectively eliminating extraneous background information.

The second preprocessing stage addressed the critical issue of intensity normalization. Recognizing the substantial variability in maximum intensity values

across different MRI volumes, a normalization scheme was implemented. Specifically, for sequences exhibiting peak intensities exceeding 800, values above the 99th percentile were clipped. The final preprocessing operation involved channel-wise Z-score standardization, ensuring consistent intensity distributions across the dataset.

nnU-Net ResENC Model: nnU-Net is a self-configuring and self-adapting deep learning framework for biomedical image segmentation [14]. It systematically optimizes preprocessing, network architecture, and training, achieving state-of-the-art performance across diverse datasets without manual tuning.

The fist segmentation pipeline implemented was based on the nnU-Net V2 framework, specifically employing a ResNet-enhanced U-Net architecture – nnU-Net ResENCM – with its default configurations [15]. For the *GLI*, *PED*, *MEN*pre, and *MET* tasks, the model processed four channel input data, comprising *T1n*, *T1c*, *T2w*, and *T2f* sequences. On the other hand, the *MEN*rt task utilized a single-channel *T1c* input. Model training was conducted over 1500 epochs, employing a 5-fold cross-validation strategy. Each epoch consisted of 250 training iterations and 50 validation iterations. The optimization process was initiated with a learning rate of 10e-2, a batch size of 3, and incorporated deep supervision.

The input patch dimensions were 128×160×112 voxels for the *GLI* and *MEN*pre tasks, 112x160x128 for *MET* and *PED*, and 96x160x160 for *MEN*rt task. All models in this pipeline featured six encoder stages, except for the *MEN*rt which included seven states of encoder blocks, initiating from 32 feature maps in the first block to 512 in the latent space. This pipeline was trained with both label-based and region-based optimization approaches.

MedNeXt Model: The second segmentation pipeline is MedNeXt [33] which leverages an architecture composed exclusively of ConvNeXt blocks [35] to capitalize on their design advantages. To maintain contextual information during upsampling and downsampling operations, the network replaces standard up-down/sample blocks with Residual Inverted Bottlenecks. Furthermore, to mitigate performance saturation commonly associated with large kernel sizes, training can be initiated with smaller kernels, which can then be progressively increased using the UpKern technique. Overall, MedNeXt functions as a scalable encoder-decoder framework optimized for 3D segmentation tasks, designed to maximize the potential of ConvNeXt architectures even when faced with the constraints of limited datasets.

In this study, we explored MedNeXt's functionality for the label-based and region-based segmentation of all the studied tumor types. Both models were trained using large-scale network architectures with a kernel size of 3x3x3, a batch size of 2, isotropic spacing of 1mm, and a patch size of 128x128x128, adhering to the nnU-Net training protocol.

Context-aware Tumor Segmentation: In recent years, numerous studies have demonstrated that the integration of contextual information into the learn-

ing process significantly enhances model learning capacity and, therefore, improves overall performance. Within the domain of deep learning for medical imaging, contextual information can be incorporated through various mechanisms, including modifications to network architecture, optimization procedures, or the explicit inclusion of relevant anatomical data [6, 36].

Concurrently, in anomaly detection applications, the primary objective is to identify deviations from learned representations of healthy anatomical structures. This implicitly categorizes image content as either healthy or abnormal [4].

Inspired by these principles, this paper proposes a segmentation strategy that includes brain tissues as an additional class, alongside tumoral regions, within the segmentation labels. The underlying hypothesis is that this approach will enable the model to not only directly segment tumoral regions but also to effectively differentiate between healthy tissues and pathological areas. This strategy can enhance the model's learning capacity by simultaneously leveraging information from both target tumors and their surrounding healthy tissues. To implement this concept, we utilized HD-BET, a rigorously validated algorithm known for its robust segmentation of brain tissues even in the presence of pathologies such as tumors [13]. By excluding the tumoral regions from the binary segmentation output of HD-BET, a new mask representing healthy brain tissue was generated. This new mask was then integrated as an additional label into the tumor label mask. Therefore, for each task, a new label was appended to the segmentation target. For example, the *MEN*rt segmentation masks were transformed from a binary to a two-class segmentation scheme. Figure 1 provides illustrative examples of the implemented strategy.

As expected, the inclusion of brain tissues as a new class introduces a highly imbalanced segmentation problem, wherein the volume of healthy tissues significantly exceeds that of the target tumoral regions. The use of conventional segmentation loss functions in such scenarios typically results in lower *Dice similarity coefficient (DSC)* values for classes with smaller regions compared to those with larger ones. To mitigate this imbalance, Kato and Hotta proposed the Adaptive t-vMF *DSC* loss [17]. Their work re-evaluated the standard *DSC* loss and demonstrated its reformulability using cosine similarity. Building upon this, their novel t-vMF *DSC* loss leverages t-vMF similarity, an extension of cosine similarity, to construct a more compact similarity loss function. The Adaptive t-vMF *DSC* loss further incorporates an algorithm that dynamically adjusts a parameter for the t-vMF similarity based on validation accuracy. This adaptability enables the model to apply more compact similarities for easily discriminable classes and broader similarities for challenging classes, thereby facilitating adaptive training based on class accuracy and ultimately improving *DSC* for imbalanced segmentation tasks. This loss function was integrated into the nnU-Net pipeline for the optimization of the ResENC-M and MedNeXt models across the evaluated datasets.

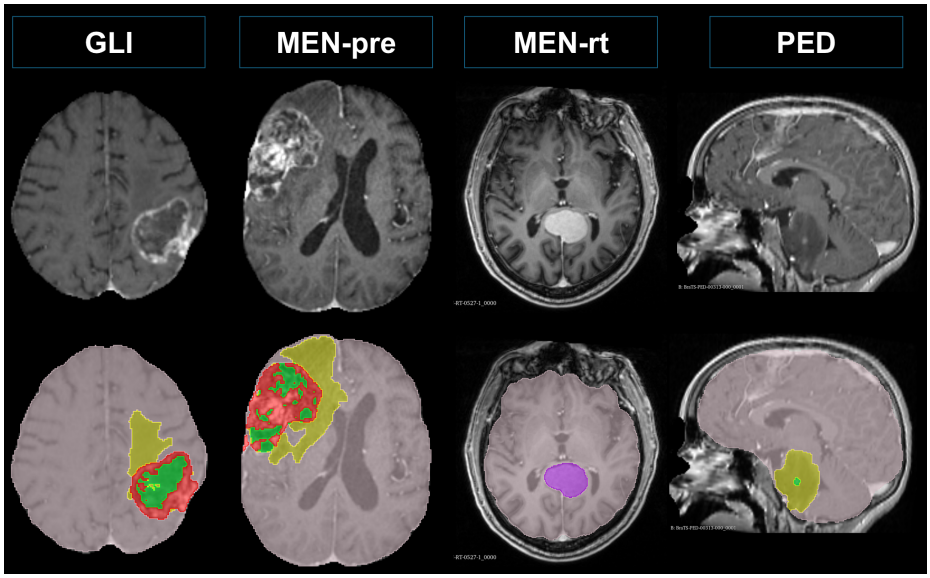

Fig. 1. Segmentation labels including healthy brain tissues alongside *GLI*, *MEN*-pre, *MEN*-rt, and *PED* samples. Tumor subregions are represented by green, blue, yellow, and red, with healthy brain tissue shown in thistle.

3 Results

The segmentation models were developed using a 5-fold cross-validation methodology on the training dataset. For simplicity and clarity, this paper only presents the quantitative *DSC* metrics. The following abbreviations will be used to denote our proposed solutions:

- B: Baseline – corresponds to segmentation models utilizing original data.
- P: Preprocessed – refers to segmentation models trained with preprocessed data.
- ML: Modified Loss – indicates segmentation models incorporating the modified loss function.
- Br: Brain tissue – denotes segmentation models leveraging brain tissue labels as contextual information.

Tables 1 through 5 present the subject-wise *DSC* metrics, showcasing the segmentation performance of the optimal results obtained across all conducted experiments. While various permutations of preprocessed datasets, the inclusion or exclusion of contextual information, diverse network architectures, and different loss functions were independently investigated and evaluated, this section only presents the highest performing configurations. Furthermore, it is noteworthy that two independent models were developed for the *GLI* task, addressing pre- and post-treatment datasets, separately.

Table 1. Quantified subject-wise *DSC* metrics for *GLI* task on the training set.

Entity	Data/Model	Architecture	Task ID	DSC ($\mu \pm \sigma$)					
				ET	**NETC**	**RC**	**SNFH**	**TC**	**WT**
Pre	B	ResENC-M	GLIpre1	0.866 ± 0.190	0.767 ± 0.271	–	0.860 ± 0.173	0.921 ± 0.136	0.929 ± 0.072
	P	ResENC-M	GLIpre2	0.877 ± 0.187	0.775 ± 0.284	–	0.870 ± 0.139	0.929 ± 0.141	0.933 ± 0.073
	P-ML	ResENC-M	GLIpre3	0.881 ± 0.169	0.781 ± 0.269	–	0.898 ± 0.170	0.929 ± 0.158	0.933 ± 0.068
	P-ML-Br	MedNeXt-L	GLIpre4	0.889 ± 0.171	0.793 ± 0.252	–	0.889 ± 0.162	0.931 ± 0.122	0.941 ± 0.065
Post	B	ResENC-M	GLIpost1	0.758 ± 0.283	0.611 ± 0.361	0.736 ± 0.272	0.907 ± 0.079	0.751 ± 0.314	0.902 ± 0.086
	P	ResENC-M	GLIpost2	0.762 ± 0.292	0.607 ± 0.354	0.758 ± 0.313	0.919 ± 0.091	0.755 ± 0.298	0.916 ± 0.090
	P-ML	ResENC-M	GLIpost3	0.749 ± 0.339	0.633 ± 0.388	0.718 ± 0.368	0.913 ± 0.083	0.706 ± 0.339	0.922 ± 0.078
	P-ML-Br	MedNeXt-L	GLIpost4	0.751 ± 0.299	0.643 ± 0.347	0.768 ± 0.298	0.911 ± 0.085	0.756 ± 0.257	0.920 ± 0.081

Table 2. Quantified subject-wise *DSC* metrics for *PED* task on the training set.

Data/Model	Architecture	Task ID	DSC ($\mu \pm \sigma$)					
			ET	**NETC**	**CC**	**SNFH**	**TC**	**WT**
B	ResENC-M	PED1	0.558 ± 0.366	0.794 ± 0.230	0.240 ± 0.347	0.160 ± 0.284	0.865 ± 0.170	0.887 ± 0.149
P	ResENC-M	PED2	0.571 ± 0.282	0.830 ± 0.218	0.310 ± 0.301	0.230 ± 0.284	0.881 ± 0.183	0.898 ± 0.135
P-ML	ResENC-M	PED3	0.601 ± 0.219	0.810 ± 0.307	0.298 ± 0.252	0.281 ± 0.158	0.879 ± 0.195	0.908 ± 0.120
P-ML-Br	MedNeXt-L	PED4	0.592 ± 0.307	0.819 ± 0.272	0.339 ± 0.287	0.268 ± 0.184	0.884 ± 0.173	0.904 ± 0.142

Table 3. Quantified subject-wise *DSC* metrics for *MET* task on the training set.

Data/Model	Architecture	Task ID	DSC ($\mu \pm \sigma$)			
			ET	**RC**	**TC**	**WT**
B	ResENC-M	MET1	0.721 ± 0.268	0.447 ± 0.402	0.751 ± 0.259	0.754 ± 0.281
P	ResENC-M	MET2	0.740 ± 0.244	0.469 ± 0.332	0.765 ± 0.255	0.774 ± 0.247
P-ML	ResENC-M	MET3	0.711 ± 0.244	0.416 ± 0.398	0.754 ± 0.282	0.750 ± 0.278
P-ML-Br	MedNeXt-L	MET4	0.732 ± 0.219	0.431 ± 0.284	0.737 ± 0.318	0.748 ± 0.321
P-ML cascade	MedNeXt-L/ResENC-M	MET5	0.692 ± 0.320	0.399 ± 0.379	0.707 ± 0.346	0.715 ± 0.254

For the *MET* task, the inclusion of brain tissue as an additional label was deemed impractical due to the often tiny size of the lesions. This disparity in class sizes led to significant imbalance, causing segmentation results to be consistently skewed towards the brain tissue, even with the application of class-adaptive loss functions. To address this challenge, a cascaded model approach was implemented. Initially, a two-class segmentation model was trained to differentiate between the union of all tumor subregions and the surrounding brain tissue. The output of this initial model underwent post-processing to generate a binary segmentation mask specifically for the metastatic regions. This mask was then incorporated as an additional input channel for a second network, which was directly optimized for the segmentation of metastases subregions.

Figure 2 details the segmentation tasks by illustrating the studied *MRI* sequences, segmentation labels, and the corresponding predicted labels for each task.

The reported metrics clearly demonstrate that including brain tissue as an additional label consistently improved segmentation accuracy across various tumor entities and their subregionse except for the *MET* task.

Quantified metrics indicate that no single configuration consistently achieved optimal accuracy across all examined regions. For instance, for the *GLI*pre

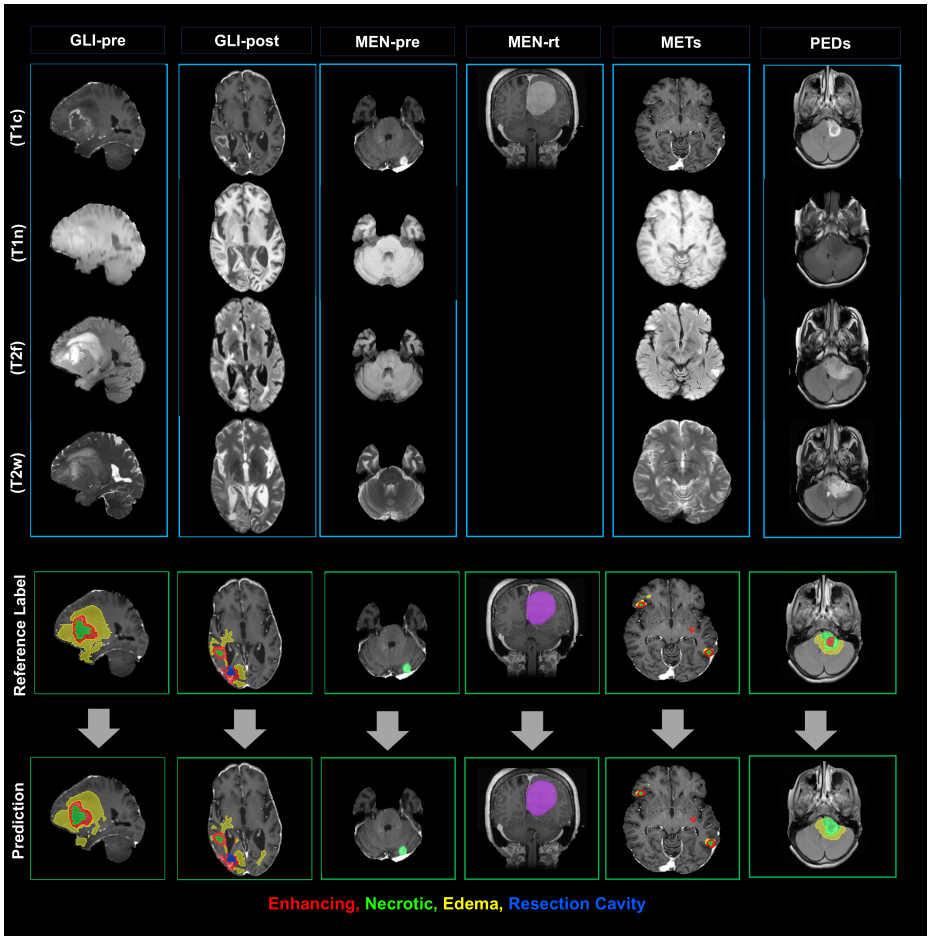

Fig. 2. Overview of studied segmentation tasks. Each column delineates a specific segmentation task, while the upper four rows indicate the corresponding MRI modalities required. Tumor subregions, including *ET*, *NETC*, *SNFH*, *RC*, *CC* and *GTV*, are depicted with distinct color-coded segmentation labels superimposed on representative 2D slices.

Table 4. Quantified subject-wise *DSC* metrics for *MEN*pre task on the training set.

Data/Model	Architecture	Task ID	DSC ($\mu \pm \sigma$)		
			ET	**TC**	**WT**
B	ResENC-M	MENpre1	0.931 ± 0.146	0.929 ± 0.147	0.919 ± 0.151
P	ResENC-M	MENpre2	0.934 ± 0.131	0.932 ± 0.138	0.919 ± 0.146
P-ML	ResENC-M	MENpre3	0.937 ± 0.134	0.935 ± 0.140	0.926 ± 0.143
P-ML-Br	ResENC-M	MENpre4	0.939 ± 0.131	0.936 ± 0.138	0.928 ± 0.142

Table 5. Quantified subject-wise *DSC* metrics for *MEN*rt task on the training set.

Data/Model	Architecture	Task ID	DSC ($\mu \pm \sigma$)
			GTV
B	ResENC-M	MENrt1	0.781 ± 0.250
P	ResENC-M	MENrt2	0.792 ± 0.241
P-ML	ResENC-M	MENrt3	0.788 ± 0.239
P-ML-Br	MedNeXt-L	MENrt4	0.795 ± 0.238

task, configuration *GLIpre4* demonstrated superior performance for the *ET* and *NETC* regions, whereas configuration *GLIpre3* yielded more accurate segmentations for the *SNFH* region. Therefore, an ensemble approach, aggregating these two models, was employed for the final *GLI*pre task.

This strategy was similarly applied to other tasks where feasible. Thus, the various Task IDs presented in Table 6 denote the instances of model aggregation employed. This table further details the optimal performance achieved from the submitted masks on the Synapse platform's validation datasets. It is important to note that the models with the configurations outlined in Table 6 were subsequently utilized as containerized algorithms for the final submission during the testing phase, under the Synapse username **Astarakee** and Synapse project ID **syn67269876**.

Table 6. Quantified lesion-wise *DSC* metrics for all the studied tasks on the validation set.

Entity	Task IDs	DSC ($\mu \pm \sigma$)					
		ET	NECT	RC/CC	SNFH/ED	TC	WT
GLI-pre	GLIpre3 GLIpre4	0.827 ± 0.230	0.748 ± 0.282	–	0.788 ± 0.203	0.840 ± 0.231	0.884 ± 0.146
GLI-post	GLIpost2 GLIpost3 GLIpost4	0.739 ± 0.305	0.797 ± 0.352	0.710 ± 0.365	0.846 ± 0.200	0.717 ± 0.305	0.861 ± 0.201
GLI-all	GLIpre3 GLIpre4 GLIpost2 GLIpost3 GLIpost4	0.786 ± 0.270	0.770 ± 0.317	0.866 ± 0.286	0.822 ± 0.204	0.783 ± 0.274	0.873 ± 0.173
PED	PED2 PED3 PED4	0.630 ± 0.427	0.917 ± 0.123	0.752 ± 0.415	0.967 ± 0.179	0.945 ± 0.107	0.945 ± 0.108
MET	MET2	0.678 ± 0.276	–	0.930 ± 0.224	–	0.695 ± 0.279	0.679 ± 0.272
MEN-pre	MENpre4	0.873 ± 0.223	–	–	–	0.886 ± 0.200	0.861 ± 0.213
MEN-rt	MENrt2 MENrt4	GTV 0.845 ± 0.165					

4 Discussion

The *BraTS* 2025 MICCAI Lighthouse challenge comprises eleven tasks, encompassing the segmentation of various brain pathologies in MRI volume which includes adult *GLI* (pre- and post-operative), *PED* glioma (pre-operative), *MEN* (pre-operative and RT planning), and *MET*.

In the last few years, while a body of literature has proposed robust solutions for medical image segmentation, including brain tumors for the *BraTS* challenge, the specific strategy of incorporating brain tissues as an additional segmentation class to enhance the distinction between normal brain tissues and tumoral regions has not been previously explored, at least to the best knowledge of the authors.

In this study, we investigated the efficacy of this novel approach when integrated into state-of-the-art models for segmenting different brain tumor entities. Our method involved simultaneously segmenting both tumoral regions and brain tissues, which necessitated modifying the loss function to accommodate the inherent imbalance in the size of these structures. The proposed pipeline incorporated a simple yet effective image preprocessing sequence, including brain tissue cropping and intensity normalization. For the segmentation models, we selected nnU-Net ResENC-M and MedNeXt due to their demonstrated superior performance in various segmentation applications. Finally, an aggregation of top-performing models from the training phase was utilized for the ultimate submission across the validation and testing phases of the challenge.

Our experiments generally demonstrate the efficacy of the proposed approach for all tasks investigated, with the exception of the *MET* task. Specifically, the inclusion of brain tissues during the training of both nnU-Net and MedNeXt models, when optimized with the modified loss function, led to improved segmentation accuracy across different tumor subregions. However, the significantly smaller size of *MET* lesions compared to the large size of brain tissue resulted in a substantial imbalance ratio, leading to poor performance for the MET task despite the modified loss function's attempt to balance this ratio during optimization.

While both ResENC and MedNeXt baseline models exhibited robust segmentation performance when applied directly to raw datasets, our findings indicate that preprocessing the datasets, providing additional contextual information during the training procedure, and subtle optimizations to the training protocols can further enhance segmentation accuracy of these models.

In summary, our contributions to the *BraTS* 2025 challenge culminated in robust segmentation models for each of the five tasks investigated, yielding competitive results on the validation sets, which were subsequently evaluated and reported on the unranked Synapse leaderboards.

Acknowledgmenet

This research was supported by the Cancer Research Funds of Radiumhemmet. The Swedish Cancer Society and The Swedish Research Council (grant number

2020-04618) are gratefully acknowledged for their support. The authors also extend their appreciation to Stockholm Medical Artificial Intelligence and Learning Environments (SMAILE) for providing access to their computational resources.

Disclosure of Interests

The authors have no competing interests to declare that are relevant to the content of this article.

Bibliography

[1] Ujjwal Baid, Satyam Ghodasara, and et. al. The rsna-asnr-miccai brats 2021 benchmark on brain tumor segmentation and radiogenomic classification, 2021. URL https://arxiv.org/abs/2107.02314.

[2] Spyridon Bakas, Hamed Akbari, Aristeidis Sotiras, Michel Bilello, Martin Rozycki, Justin S. Kirby, John B. Freymann, Keyvan Farahani, and Christos Davatzikos. Advancing the cancer genome atlas glioma mri collections with expert segmentation labels and radiomic features. *Scientific Data*, 4(1): 170117, Sep 2017. https://doi.org/10.1038/sdata.2017.117.

[3] Spyridon Bakas, Mauricio Reyes, Andras Jakab, Stefan Bauer, Markus Rempfler, and et al Alessandro Crimi. Identifying the best machine learning algorithms for brain tumor segmentation, progression assessment, and overall survival prediction in the brats challenge, 2019. URL https://arxiv.org/abs/1811.02629.

[4] Christoph Baur, Stefan Denner, Benedikt Wiestler, Nassir Navab, and Shadi Albarqouni. Autoencoders for unsupervised anomaly segmentation in brain mr images: A comparative study. *Medical Image Analysis*, 69:101952, 2021. ISSN 1361-8415. https://doi.org/https://doi.org/10.1016/j.media.2020.101952. URL https://www.sciencedirect.com/science/article/pii/S1361841520303169.

[5] Maria Correia de Verdier and Rachit Saluja et. al. The 2024 brain tumor segmentation (brats) challenge: Glioma segmentation on post-treatment mri, 2024. URL https://arxiv.org/abs/2405.18368.

[6] Shuanglang Feng, Heming Zhao, Fei Shi, Xuena Cheng, Meng Wang, Yuhui Ma, Dehui Xiang, Weifang Zhu, and Xinjian Chen. Cpfnet: Context pyramid fusion network for medical image segmentation. *IEEE Transactions on Medical Imaging*, 39(10):3008–3018, 2020. https://doi.org/10.1109/TMI.2020.2983721.

[7] André Ferreira, Naida Solak, Jianning Li, Philipp Dammann, Jens Kleesiek, Victor Alves, and Jan Egger. How we won brats 2023 adult glioma challenge? just faking it! enhanced synthetic data augmentation and model ensemble for brain tumour segmentation, 2024. URL https://arxiv.org/abs/2402.17317.

[8] VS Fonov, AC Evans, RC McKinstry, CR Almli, and DL Collins. Unbiased nonlinear average age-appropriate brain templates from birth to adulthood. *NeuroImage*, 47:S102, 2009. ISSN 1053-8119. https://doi.org/https://doi.org/10.1016/S1053-8119(09)70884-5. URL https://www.sciencedirect.com/science/article/pii/S1053811909708845. Organization for Human Brain Mapping 2009 Annual Meeting.

[9] S. Growcott, T. Dembrey, R. Patel, D. Eaton, and A. Cameron. Inter-observer variability in target volume delineations of benign and metastatic brain tumours for stereotactic radiosurgery: Results of a national quality assurance programme. *Clinical Oncology*, 32(1):13–25, 2020. ISSN

0936-6555. https://doi.org/https://doi.org/10.1016/j.clon.2019.06.015. URL https://www.sciencedirect.com/science/article/pii/S0936655519302766.

[10] Ali Hatamizadeh, Vishwesh Nath, Yucheng Tang, Dong Yang, Holger R. Roth, and Daguang Xu. Swin unetr: Swin transformers for semantic segmentation of brain tumors in mri images. In Alessandro Crimi and Spyridon Bakas, editors, *Brainlesion: Glioma, Multiple Sclerosis, Stroke and Traumatic Brain Injuries*, pages 272–284, Cham, 2022. Springer International Publishing.

[11] Leland S. Hu, Andrea Hawkins-Daarud, Lujia Wang, Jing Li, and Kristin R. Swanson. Imaging of intratumoral heterogeneity in high-grade glioma. *Cancer Letters*, 477:97–106, May 2020.

[12] Ziyan Huang, Haoyu Wang, Zhongying Deng, Jin Ye, Yanzhou Su, Hui Sun, Junjun He, Yun Gu, Lixu Gu, Shaoting Zhang, and Yu Qiao. Stu-net: Scalable and transferable medical image segmentation models empowered by large-scale supervised pre-training, 2023. URL https://arxiv.org/abs/2304.06716.

[13] Fabian Isensee, Marianne Schell, Irada Pflueger, Gianluca Brugnara, David Bonekamp, Ulf Neuberger, Antje Wick, Heinz-Peter Schlemmer, Sabine Heiland, Wolfgang Wick, Martin Bendszus, Klaus H. Maier-Hein, and Philipp Kickingereder. Automated brain extraction of multisequence mri using artificial neural networks. *Human Brain Mapping*, 40(17):4952–4964, 2019. https://doi.org/https://doi.org/10.1002/hbm.24750.

[14] Fabian Isensee, Paul F. Jaeger, Simon A. A. Kohl, Jens Petersen, and Klaus H. Maier-Hein. nnu-net: a self-configuring method for deep learning-based biomedical image segmentation. *Nature Methods*, 18(2):203–211, Feb 2021. ISSN 1548-7105. https://doi.org/10.1038/s41592-020-01008-z.

[15] Fabian Isensee, Tassilo Wald, Constantin Ulrich, Michael Baumgartner, Saikat Roy, Klaus Maier-Hein, and Paul F. Jaeger. nnu-net revisited: A call for rigorous validation in 3d medical image segmentation, 2024. URL https://arxiv.org/abs/2404.09556.

[16] Alexandros Karargyris, Renato Umeton, Micah J. Sheller, and et al. Federated benchmarking of medical artificial intelligence with medperf. *Nature Machine Intelligence*, 5(7):799–810, Jul 2023. https://doi.org/10.1038/s42256-023-00652-2.

[17] Sota Kato and Kazuhiro Hotta. Adaptive t-vmf dice loss: An effective expansion of dice loss for medical image segmentation. *Computers in Biology and Medicine*, 168:107695, 2024. ISSN 0010-4825. https://doi.org/https://doi.org/10.1016/j.compbiomed.2023.107695. URL https://www.sciencedirect.com/science/article/pii/S0010482523011605.

[18] Anahita Fathi Kazerooni and Nastaran Khalili et. al. The brain tumor segmentation (brats) challenge 2023: Focus on pediatrics (cbtn-connect-dipgr-asnr-miccai brats-peds), 2024. URL https://arxiv.org/abs/2305.17033.

[19] Anahita Fathi Kazerooni, Nastaran Khalili, and et al. The brain tumor segmentation in pediatrics (brats-peds) challenge: Focus on pediatrics (cbtn-

connect-dipgr-asnr-miccai brats-peds), 2024. URL https://arxiv.org/abs/2404.15009.

[20] Dominic LaBella and Maruf Adewole et. al. The asnr-miccai brain tumor segmentation (brats) challenge 2023: Intracranial meningioma, 2023. URL https://arxiv.org/abs/2305.07642.

[21] Dominic LaBella, Valeriia Abramova, and Mehdi Astaraki et. al. Analysis of the 2024 brats meningioma radiotherapy planning automated segmentation challenge, 2025. URL https://arxiv.org/abs/2405.18383.

[22] Huan Minh Luu and Sung-Hong Park. Extending nn-unet for brain tumor segmentation. In Alessandro Crimi and Spyridon Bakas, editors, *Brainlesion: Glioma, Multiple Sclerosis, Stroke and Traumatic Brain Injuries*, pages 173–186, Cham, 2022. Springer International Publishing.

[23] Jun Ma, Feifei Li, and Bo Wang. U-mamba: Enhancing long-range dependency for biomedical image segmentation, 2024. URL https://arxiv.org/abs/2401.04722.

[24] Nazanin Maleki and Raisa Amiruddin et. al. Analysis of the miccai brain tumor segmentation – metastases (brats-mets) 2025 lighthouse challenge: Brain metastasis segmentation on pre- and post-treatment mri, 2025. URL https://arxiv.org/abs/2504.12527.

[25] Bjoern Menze, Fabian Isensee, Roland Wiest, Bene Wiestler, Klaus Maier-Hein, Mauricio Reyes, and Spyridon Bakas. Analyzing magnetic resonance imaging data from glioma patients using deep learning. *Computerized Medical Imaging and Graphics*, 88:101828, 2021. ISSN 0895-6111. https://doi.org/https://doi.org/10.1016/j.compmedimag.2020.101828. URL https://www.sciencedirect.com/science/article/pii/S0895611120301233.

[26] Bjoern H. Menze, Andras Jakab, and et al Bauer. The multimodal brain tumor image segmentation benchmark (brats). *IEEE Transactions on Medical Imaging*, 34(10):1993–2024, 2015. https://doi.org/10.1109/TMI.2014.2377694.

[27] Fausto Milletari, Nassir Navab, and Seyed-Ahmad Ahmadi. V-net: Fully convolutional neural networks for volumetric medical image segmentation. In *2016 Fourth International Conference on 3D Vision (3DV)*, pages 565–571, 2016. https://doi.org/10.1109/3DV.2016.79.

[28] Ahmed W. Moawad, Anastasia Janas, and et. al. The brain tumor segmentation (brats-mets) challenge 2023: Brain metastasis segmentation on pre-treatment mri, 2024. URL https://arxiv.org/abs/2306.00838.

[29] Andriy Myronenko. 3d mri brain tumor segmentation using autoencoder regularization. In Alessandro Crimi, Spyridon Bakas, Hugo Kuijf, Farahani Keyvan, Mauricio Reyes, and Theo van Walsum, editors, *Brainlesion: Glioma, Multiple Sclerosis, Stroke and Traumatic Brain Injuries*, pages 311–320, Cham, 2019. Springer International Publishing.

[30] Quinn T. Ostrom, Stephen S. Francis, and Jill S. Barnholtz-Sloan. Epidemiology of brain and other cns tumors. *Current Neurology and Neuroscience Reports*, 21(12):68, Nov 2021. ISSN 1534-6293. https://doi.

org/10.1007/s11910-021-01152-9. URL https://doi.org/10.1007/s11910-021-01152-9.

[31] Torsten Rohlfing, Natalie M Zahr, Edith V Sullivan, and Adolf Pfefferbaum. The sri24 multichannel atlas of normal adult human brain structure. *Human brain mapping*, 31(5):798–819, 2010.

[32] Olaf Ronneberger, Philipp Fischer, and Thomas Brox. U-net: Convolutional networks for biomedical image segmentation. In Nassir Navab, Joachim Hornegger, William M. Wells, and Alejandro F. Frangi, editors, *Medical Image Computing and Computer-Assisted Intervention – MICCAI 2015*, pages 234–241, Cham, 2015. Springer International Publishing.

[33] Saikat Roy, Gregor Koehler, Constantin Ulrich, Michael Baumgartner, Jens Petersen, Fabian Isensee, Paul F. Jäger, and Klaus H. Maier-Hein. Mednext: Transformer-driven scaling of convnets for medical image segmentation. In Hayit Greenspan, Anant Madabhushi, Parvin Mousavi, Septimiu Salcudean, James Duncan, Tanveer Syeda-Mahmood, and Russell Taylor, editors, *Medical Image Computing and Computer Assisted Intervention – MICCAI 2023*, pages 405–415, Cham, 2023. Springer Nature Switzerland.

[34] Saikat Roy, Gregor Koehler, Constantin Ulrich, Michael Baumgartner, Jens Petersen, Fabian Isensee, Paul F. Jaeger, and Klaus Maier-Hein. Mednext: Transformer-driven scaling of convnets for medical image segmentation, 2024. URL https://arxiv.org/abs/2303.09975.

[35] Sanghyun Woo, Shoubhik Debnath, Ronghang Hu, Xinlei Chen, Zhuang Liu, In So Kweon, and Saining Xie. Convnext v2: Co-designing and scaling convnets with masked autoencoders, 2023. URL https://arxiv.org/abs/2301.00808.

[36] Xiwang Xie, Weidong Zhang, Xipeng Pan, Lijie Xie, Feng Shao, Wenyi Zhao, and Jubai An. Canet: Context aware network with dual-stream pyramid for medical image segmentation. *Biomedical Signal Processing and Control*, 81:104437, 2023. ISSN 1746-8094. https://doi.org/https://doi.org/10.1016/j.bspc.2022.104437. URL https://www.sciencedirect.com/science/article/pii/S1746809422008916.

[37] Ramy A. Zeineldin, Mohamed E. Karar, Oliver Burgert, and Franziska Mathis-Ullrich. Multimodal cnn networks for brain tumor segmentation in mri: A brats 2022 challenge solution. In Spyridon Bakas, Alessandro Crimi, Ujjwal Baid, Sylwia Malec, Monika Pytlarz, Bhakti Baheti, Maximilian Zenk, and Reuben Dorent, editors, *Brainlesion: Glioma, Multiple Sclerosis, Stroke and Traumatic Brain Injuries*, pages 127–137, Cham, 2023. Springer Nature Switzerland.

[38] Zongwei Zhou, Md Mahfuzur Rahman Siddiquee, Nima Tajbakhsh, and Jianming Liang. Unet++: Redesigning skip connections to exploit multiscale features in image segmentation, 2020. URL https://arxiv.org/abs/1912.05074.